The flow of a foam in a two-dimensional porous medium

Baudouin Géraud, Siân A. Jones, Isabelle Cantat, Benjamin Dollet, Yves Méheust

AGU PUBLICATIONS

Water Resources Research

RESEARCH ARTICLE

10.1002/2015WR017936

The flow of a foam in a two-dimensional porous medium

Baudouin Géraud[1], Siân A. Jones[1], Isabelle Cantat[1], Benjamin Dollet[1], and Yves Méheust[2]

[1]Institut de Physique de Rennes, UMR CNRS 6251, Université Rennes 1, Rennes, France, [2]Géosciences Rennes, UMR CNRS 6118, Université Rennes 1, Rennes, France

Key Points:
- We study the flow of a 2-D foam in a porous medium and monitor the bubble sizes *A* and velocities *V*
- We observe preferential and intermittent flow, bubble fragmentation, and correlation between *A* and *V*
- Large-scale models of subsurface foam flows may have to take this correlation into account

Correspondence to:
Y. Méheust,
yves.meheust@univ-rennes1.fr

Citation:
Géraud, B., S. A. Jones, I. Cantat, B. Dollet, and Y. Méheust (2016), The flow of a foam in a two-dimensional porous medium, *Water Resour. Res.*, *52*, doi:10.1002/2015WR017936.

Received 31 JUL 2015
Accepted 27 DEC 2015
Accepted article online 30 DEC 2015

Abstract Foams have been used for decades as displacing fluids for enhanced oil recovery and aquifer remediation, and more recently, for remediation of the vadose zone, in which case foams carry chemical amendments. Foams are better injection fluids than aqueous solutions due to their low sensitivity to gravity and because they are less sensitive to permeability heterogeneities, thus allowing a more uniform sweep. The latter aspect results from their peculiar rheology, whose understanding motivates the present study. We investigate foam flow through a two-dimensional porous medium consisting of circular obstacles positioned randomly in a horizontal transparent Hele-Shaw cell. The local foam structure is recorded in situ, which provides a measure of the spatial distribution of bubble velocities and sizes at regular time intervals. The flow exhibits a rich phenomenology including preferential flow paths and local flow nonstationarity (intermittency) despite the imposed permanent global flow rate. Moreover, the medium selects the bubble size distribution through lamella division-triggered bubble fragmentation. Varying the mean bubble size of the injected foam, its water content, and mean velocity, we characterize those processes systematically. In particular, we measure the spatial evolution of the distribution of bubble areas, and infer the efficiency of bubble fragmentation depending on the various control parameters. We furthermore show that the distributions of bubble sizes and velocities are correlated. This study sheds new light on the local rheology of foams in porous media and opens the way toward quantitative characterization of the relationship between medium geometry and foam flow properties. It also suggests that large-scale models of foam flows in the subsurface should account for the correlation between bubble sizes and velocities.

1. Introduction

Aqueous foams consist of air bubbles separated by films of an aqueous solution [*Weaire and Hutzler*, 1999; *Cantat et al.*, 2013] that contain surfactants to lower the surface tension. They are used in a number of industrial applications, including glass manufacturing, ore flotation, or firefighting technology [*Stevenson*, 2012]. Enhanced oil recovery (EOR) has been the first application for subsurface environments: injection of surfactant together with gas into the subsurface has been used as early as 50 years ago [*Patzek*, 1996] to generate foam in situ and improve oil sweep, in particular, in the framework of steam EOR [*Zhdanov et al.*, 1996]. More recently, foams have been used to remediate aquifers contaminated with nonaqueous phase liquids (NAPLs), in a manner very similar to EOR [*Hirasaki et al.*, 1997]. In both applications, the use of foams offers the following advantages: a reduction by 1 order of magnitude in the needed volume of solution for a given injection volume, since only about 10% of the foam consists of liquid solution, the rest being gas; a reduction of the needed amount of surfactant [*Roy et al.*, 1995a, 1995b], a better sweep of the defending fluid due to a more favorable mobility ratio with respect to the oil [*Huang et al.*, 1986], and diversion mechanisms resulting from the particular dissipation mechanisms at play when a foam flows through a porous medium: the foam tends to first occupy large permeability regions, where its low mobility causes later flow to sweep low-permeability regions [*Szafranski et al.*, 1998; *Huang and Chang*, 2000; *Jeong et al.*, 2000; *Jeong and Corapcioglu*, 2003].

A more recent application, which motivates the present study, is the remediation of vadose zone environments, and particularly of soils [*Chowdiah et al.*, 1998; *Jeong et al.*, 2000; *Wang and Mulligan*, 2004; *Zhong et al.*, 2010; *Shen et al.*, 2011; *Zhong et al.*, 2011]. In this context, the foam is used as carrier fluid for chemical amendments rather than as displacing fluid. In this respect, foams offer several advantages: they can be injected while maintaining a low water content in the treated zones, which is cheaper and particularly useful

for remediation of the vadose zone [*Zhong et al*., 2010]; their capacity to transport soil/colloidal particles [*Shen et al*., 2011] and bacteria [*Wan et al*., 1994] at air-water interfaces is high; transport of air along with the aqueous solution may enhance the efficiency of biodegradation [*Rothmel et al*., 1998; *Jenkins et al*., 1993]; in the case of in situ stabilization (of heavy metals, for example), a foam does not displace the target chemicals as much as a solution [*Zhong et al*., 2009, 2011]; they present a better sweeping efficiency than aqueous solutions due to a moderate sensitivity to gravity [*Zhong et al*., 2011]. In column experiments, a breaking of the foam front and consequent propagation of a wetting front ahead of the foam, which may help to optimally deliver the amendments in case of a heterogeneous reaction, has also been reported [*Zhong et al*., 2010].

The flow of bulk foams has been the subject of a vast amount of literature through the years [*Heller and Kuntamukkula*, 1987; *Weaire*, 2008; *Dollet and Raufaste*, 2014]. It occurs through sudden topological events allowing bubble rearrangement. Viscous dissipation within the films/lamellae is thus the dominant dissipation mechanism, resulting in a Herschel-Bulkley rheology; a yield stress σ_y must be overcome for the foam to start flowing, and the rheology under shear is shear thinning:

$$\sigma = \sigma_y + K\,\dot{\gamma}^n\,, \tag{1}$$

where σ is the shear stress, K the consistency, $\dot{\gamma}$ the strain rate, and the exponent n lies in the range [0.2; 0.4] [*Denkov et al*., 2005].

In contrast to bulk flow, when a foam flows inside a porous medium whose channels/dimensions are of the same order as the bubble size, a large part of the dissipation occurs in the wall films and in the Plateau borders that connect these films to the lamellae separating the flowing bubbles. Consequently, the foam rheology is expected to be different from that of bulk foam. Moreover, it strongly depends on the relative sizes of the pores and foam bubbles [*Heller and Kuntamukkula*, 1987]. The mobility of foams through porous media can be expressed in a manner similar to that of Newtonian fluids, using Darcy's law to relate the drop in hydraulic head over a length L of medium, Δh, to the apparent mean velocity, or Darcy velocity, v_d. The standard form of that law is $v_d = (\kappa\,\rho\,g/\mu)(\Delta h/L)$, where κ is the intrinsic permeability of the medium, ρ the mass density of the fluid, and μ its viscosity. For foam flow, it has been proposed that a Darcy law can be written provided that μ is replaced by an effective viscosity $\mu_{\text{eff}} = \mu_g + \beta/v^{1/3}$ [*Friedmann et al*., 1991; *Kovscek and Bertin*, 2003a], where μ_g is the gas viscosity, β is a parameter that depends on the medium geometry, on the foam formulation, and on its texture (that is, its average bubble size), and $v = v_d/\phi$ is the interstitial velocity, ϕ being the porosity of the medium. Combining the expression for the effective viscosity with Darcy's law and neglecting the gas viscosity yields a nonlinear relationship between the pressure and mean interstitial velocity:

$$v = \left(\frac{\kappa}{\beta\,\phi}\right)^{3/2}\left[\frac{\Delta(p+\rho\,g\,z)}{L}\right]^{3/2}, \tag{2}$$

where we have introduced the pressure p and altitude z. Note that the foam mobility through soils, $\kappa\,\rho\,g/\mu_{\text{eff}}$, has been measured to be relatively independent of the soil permeability, and when a dependence existed, the foam's mobility was observed to decrease with increasing soil permeability [*Chowdiah et al*., 1998].

For subsurface applications, the foam is usually generated in situ, by joint injection of surfactant solution and gas. In this framework, the gas is not present everywhere in the medium. The foam is then a dispersion of gas bubbles in a liquid, where the liquid is continuous and part of the gas is made discontinuous by liquid films [*Hirasaki and Lawson*, 1985]. The part of the gas that is not made discontinuous is trapped, while the rest flows as a continuous gas phase. The trapped gas phase represents a very large part (up to 70% or 80%) of the total gas present in the medium [*Kovscek and Radke*, 1994]. *Strong foams* are foams for which a significant part of the flowing gas is discontinuous, so that flow involves the costly displacement of liquid lamellae, rendering the mobility of the gas-liquid mixture much smaller than that of the gas alone. On the contrary, foams for which most of the gas is flowing as a continuous phase are called *weak foams*. What controls whether a foam is strong or weak is a complex issue, but the mean flow velocity and surfactant formulation [*Aronson et al*., 1994] play an important role. The mobilization and trapping of bubbles have been observed to be intermittent processes, due to the existence of preferential flow paths that change in time [*Kovscek and Radke*, 1994; *Cohen et al*., 1997]. Increasing the pressure head increases the portion of gas that

is flowing and renders the foam rheology shear thinning [*Hirasaki and Lawson*, 1985; *Falls et al*., 1989]. In this regime, where the discontinuous gas phase grows or shrinks depending on the applied pressure head, foam texture is the main control parameter for the foam mobility. In this respect, three fundamental mechanisms of lamella/film creation occur during foam generation within a porous medium: *leave-behind*, in which two gas fingers invade two adjacent and communicating liquid-filled pores, trapping a film of liquid in-between them after the pores have been fully invaded; *capillary snap-off*, in which the snap-off of liquid films at the throat between two pores separates a gas bubble in two [*Roof et al*., 1970; *Gauglitz and Radke*, 1990; *Kovscek and Radke*, 1994; *Kovscek et al*., 2007]; *lamella division*, in which a liquid film touching a solid grain while still attached to other grains on this perimeter separates into two films that travel on either side of the dividing grain [*Kovscek and Radke*, 1994]. Mechanisms of bubble disappearance are also at play when a foam flows through a porous medium; they consist mostly in (i) coarsening through gas diffusion and (ii) bubble coalescence by capillary suction. Bubble coarsening results from the diffusion of gas from smaller bubbles where the pressure and chemical potential are larger, to neighboring larger bubbles; it has been studied extensively in the context of bulk foams [*Cantat et al*., 2013]. In porous media, it is observed at locations where bubbles are trapped [*Kovscek and Radke*, 1994]. Bubble coalescence by capillary suction involves the sudden rupture of a lamella; it occurs when a lamella/film that has been sitting at a pore throat is displaced quickly into a pore volume much wider than the throat, and cannot adjust its liquid volume sufficiently fast to avoid rupturing [*Khatib et al*., 1988].

The impact of foam texture or structure on the pressure drop across a porous medium, and, consequently, on flow through that medium, has also been examplified in experimental and theoretical studies performed on systems of aqueous films confined in simple geometries: single film flowing across a biconical pore [*Rossen*, 1990; *Cox et al*., 2004; *Ferguson and Cox*, 2013], single bubble [*Bretherton*, 1961], or bubble trains [*Cantat et al*., 2004; *Terriac et al*., 2006] flowing in capillaries, two-dimensional monodisperse foams of various structures (e.g., staircase structures) flowing in a single channel [*Raven and Marmottant*, 2009; *Marmottant and Raven*, 2009], in parallel channels of different widths [*Jones et al*., 2013], or in parallel convergent-divergent channels [*Dollet et al*., 2014]. Note also that the reverse also holds: given confining shapes can select particular foam structures [*Drenckhan et al*., 2005]. Already in the seminal study by *Bretherton* [1961], a scaling of the pressure drop ΔP along the medium as a function of the mean foam velocity V in the form $\Delta P \propto V^{2/3}$ was demonstrated; it was later generalized to the more complex configurations mentioned above [*Cantat et al*., 2004; *Terriac et al*., 2006; *Raufaste et al*., 2009; *Jones et al*., 2013; *Dollet et al*., 2014]. Such a scaling is perfectly consistent with rheology measurements performed at the scale of a soil column or rock core and described by equation (2) above.

While much is already known qualitatively on the mechanisms of foam displacement in porous media, and many existing macroscopic models [e.g., *Kovscek and Radke*, 1994; *Kovscek et al*., 1995; *Fergui et al*., 1998; *Kornev et al*., 1999; *Alvarez et al*., 2001; *Kam et al*., 2003; *Dholkawala et al*., 2007] address the generation and macroscopic displacement of foams in porous media, experimental studies usually involve the use of core flooding units [*Fergui et al*., 1998; *Apaydin and Kovscek*, 2001; *Pang*, 2010] from which it is difficult to obtain detailed information on the local foam structure: only global quantities can be measured, and only qualitative information on local displacement dynamics is inferred. In recent years, experiments using X-ray microtomography [*Apaydin and Kovscek*, 2001; *Zitha et al*., 2006; *Nguyen et al*., 2007; *Du et al*., 2008; *Simjoo et al*., 2012] or γ ray attenuation [*Fergui et al*., 1998] have enabled limited visualization of foam flow, revealing regions of preferential occupation of the medium by the foam and providing spatially resolved measurement of liquid fractions, also under conditions of oil sweep [*Simjoo et al*., 2013]. Experiments based on micromodels consisting of pore networks [*Jeong et al*., 2000; *Chen et al*., 2005; *Ma et al*., 2012; *Jeong and Corapcioglu*, 2003], on the other hand, have mainly been used to investigate oil or NAPL sweep, and have not allowed precise bubble-scale observation of the foam kinematics, or only on a small subpart of the system [*Jeong and Corapcioglu*, 2005], for example, in order to assess the role of capillary snap-off on foam generation [*Kovscek et al*., 2007].

In this paper, we present a series of experiments performed on a transparent two-dimensional porous medium consisting of cylindrical grains. The setup allows for full in situ time-resolved measurement of the foam structure as well as of the bubble size and individual velocities, at the expense of dimensional reduction. Previous studies on analogous models with more simple geometries have evidenced the importance of foam structure on the distribution of flows between two parallel linear channels [*Jones et al*., 2013] and the potential impact of elastic effects on the foam mobility [*Dollet et al*., 2014]. In the following, we focus on flow characteristics already known from the literature but to our knowledge never addressed

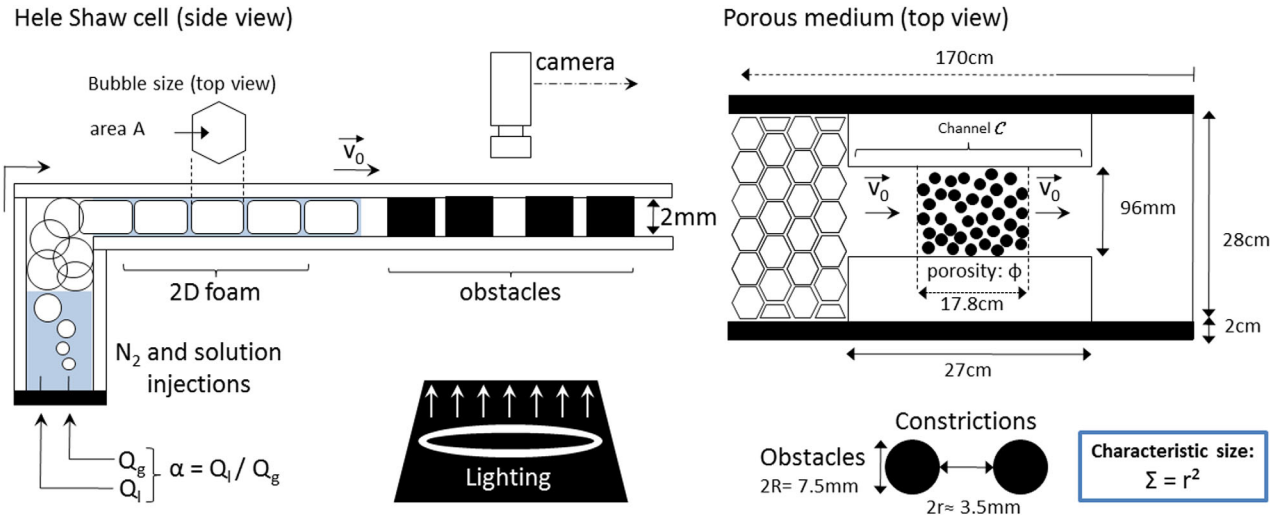

Figure 1. Sketch of the experimental setup: (left) side view and (right) top view.

experimentally with quantitative measurements: preferential flow and its relationship to the velocity probability density distribution, flow intermittency, and dynamics of the bubble size distribution. We inject into the medium a preexisting foam, so no continuous gas phase is present in our system.

The experimental methods are described in detail in section 2, while section 3 is devoted to a presentation and discussion of the results. In section 4, we summarize the findings and conclude.

2. Methods

2.1. Experimental Setup

We used an apparatus derived from the one described by *Jones et al*. [2013] (see Figure 1). The flow cell is a 170 $\times$ 32 cm^2 Hele-Shaw cell with a gap $h = 2$ mm between the glass plates. Obstacles positioned inside the Hele-Shaw cell define the pore geometry. The cell is enlightened by a circular fluorescent tube of diameter 37 cm, placed on a dark background and beneath the porous medium so as to optimize the contrast of foam films on the images. The foam structure is recorded at a regular time interval using a camera with a 1312 $\times$ 1082 resolution (Photon Focus, Alliance Vision). The acquisition rate is chosen according to the imposed flow rate and ranges from 5 to 100 Hz.

In the present study, the grains of the two-dimensional porous medium consist of monodisperse cylinders of diameter $2R = 7.5$ mm and of height equal to the cell thickness h, placed inside a narrow channel $\mathcal{C}$ near the outlet of the cell. The Hele-Shaw cell thus contains a two-dimensional porous medium. The channel $\mathcal{C}$ is 9.6 cm wide and 27 cm long, 17.8 cm of the length containing cylindrical grains. The obstacle positions were defined from a computer-generated geometry obtained by perturbing a diagonal regular mesh with a random displacement drawn from a Gaussian distribution; the process ensured that the porous medium always had a porosity $\phi = 0.5 \pm 0.02$.

2.2. Foam Generation and Flow

The foam is produced by injecting gas into a reservoir saturated with a foaming solution. A foam thus grows inside the reservoir and is displaced into the Hele-Shaw cell (see Figure 1). As they enter the cell, bubbles are squeezed between the top and bottom plates so that they are only separated from each other by vertical films (lamellae).

We used two kinds of foaming solutions in order to probe the influence of the film interfaces on the flows. We dissolved two kinds of sodium dodecyl sulfate (SDS) powders in water, one 99.9% pure and the other one 98.5% pure (Aldrich). Solution type 1 ($ST = 1$) refers to a solution obtained by dissolving 98.5% SDS in ultrapure water, solution type 2 ($ST = 2$) to one obtained from 99.9% SDS and ultrapure water. These solutions were prepared at the same surfactant concentration of 10 g/L.

Monodisperse foams are obtained by blowing nitrogen in the foaming solution at moderate gas flow rates ($Q_g \leq 200$ mL/min). The bubbles entrain the liquid from the reservoir as they leave it to enter the flow cell; we could measure the liquid flow rate Q_l from the decrease of the solution level in the reservoir with time. The resulting flux ratio $\alpha = Q_l/Q_g$ was on the order of a few percents, corresponding to what we qualify as *dry foams*. We also produced *wet* foams ($\alpha \simeq 10\%$) by injecting the solution into the cell using a peristaltic pump. These two techniques allowed us to investigate the behavior of foams of various liquid fractions ϕ_l and obtained from different surfactant solutions. Note that the *foam quality* $1-\phi_l$ is commonly used to characterize the amount of water within the foam.

The pressure variations in the cell remain orders of magnitude smaller than the atmospheric pressure. Consequently, the gas is safely assumed incompressible. In steady state, the volumetric fluxes of gas and liquid are thus uniform in the cell. The volumetric liquid fraction ϕ_l and the mean velocities $\langle v_l \rangle$ and $\langle v_g \rangle$ of the liquid and gas phases, respectively, are related to the flux ratio α as follows:

$$\alpha = \frac{\phi_l \langle v_l \rangle}{(1-\phi_l)\langle v_g \rangle} . \tag{3}$$

For comparable velocities and small liquid fractions, we would thus approximate $\alpha \simeq \phi_l$. In contrast to the mean gas velocity, however, the mean velocity of the liquid phase, $\langle v_l \rangle$, may differ from the measured bubble velocities and cannot be directly deduced from it. The liquid velocity is expected to be smaller than $\langle v_g \rangle$ in the wetting films on the top and bottom plates and larger than $\langle v_g \rangle$ in the meniscus network [*Wong et al.*, 1995]. Hence the parameters α and ϕ_l are a priori different, even though strongly correlated, and ϕ_l cannot be easily known. In the following, we therefore resort to the well-controlled experimental parameter α to characterize the foams, which are also identified by their solution type.

The length of the Hele-Shaw cell allows us to first produce the foam and fill the first part of the Hele-Shaw cell (see Figure 1) and then push this foam into the second part of the cell, where the obstacles are located. The gas and liquid fluxes Q_g and Q_l refer to the fluxes during the foam production, not during the measure. Q_g essentially defines the bubble size and Q_l/Q_g the liquid fraction. The gas flux is then modified to obtain the desired mean foam velocity. Bubble sizes and velocities were computed from image processing of the movies as explained in the following.

2.3. Image Treatment and Analysis

Images recorded at regular time intervals were analyzed using a custom made Matlab program. The processing consists of two parts: (i) the characterization of the porous medium and (ii) the analysis of the foam structure in time. The important steps of the entire process are shown in Figure 2, on a portion of the porous medium for clarity. Figure 2a shows a portion of a raw image. The white disks are the solid grains, while the dark polygons denote patches of double-sided bonding tape that are used to glue some of the grains to the Hele-Shaw cell. These polygons have been removed from all the foam structure snapshots that appear later in this article. Before each flow experiment, a picture of the empty 2-D porous medium is

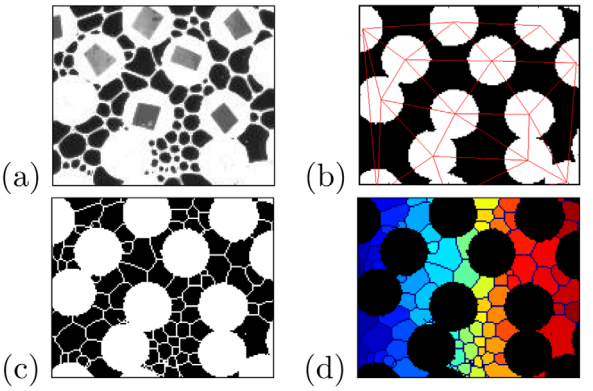

Figure 2. Successive steps in the image treatment: (a) raw image of the foam; (b) mask image defining the grains, with corresponding Delaunay triangulation superimposed; (c) binary image obtained from thresholding and skeletonizing the raw image (Figure 2a), and finally superimposing the mask (Figure 2b); (d) image with the different bubbles identified by different colors.

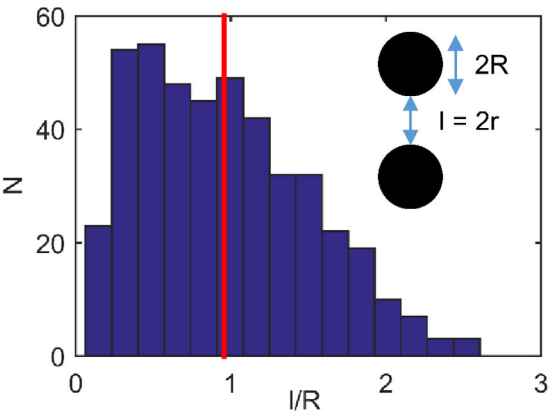

Figure 3. Distribution of the constriction widths *l* between neighbor obstacles. From this distribution, we define the length scale $r=\langle l\rangle/2$, which corresponds to the critical radius for a bubble to pass through a constriction without being deformed.

recorded. The binarization of this picture provides a "mask" that defines the geometry of the porous (and solid) space (see Figure 2b). This porous configuration is then characterized in the following manner. First, the positions of the entrance and exit of the porous medium are defined as the first and last segments perpendicular to the channel axis and that touch an obstacle. This definition then allows for a consistent measurement of the porosity. Second, a Delaunay triangulation provides the nearest neighbor obstacles for each grain, and consequently the *constriction* sizes, i.e., the distances *l* between nearest neighbors. The distribution of *l* is shown in Figure 3. We then define the distance *r* from the average value of *l*, as $r=\langle l\rangle/2$. This characteristic length scale of the disordered pore geometry is important for the foam flow process, since it corresponds to the critical radius of a bubble passing through the constriction without being deformed. We further define a characteristic size $\Sigma=r^2$, which we shall use to compare the bubble sizes to the geometry of the medium. In our experimental setup, we have $\Sigma \approx 3.2 \pm 0.3$ mm^2. For each flow image, the foam structure and dynamics are obtained through the following steps. First, the contrast is enhanced and the image is thresholded into a black and white image in which only the soap films and the obstacles remain visible. This image is then skeletonized, that is, all film widths are reduced to one pixel (Figure 2c). Note that the film width that is apparent on the raw picture is not the actual film width in the mid-plane of the cell, it corresponds rather to the transverse extent of the Plateau borders between the vertical films and the film that wets the cell's top plate; choosing a film width of one pixel is somewhat arbitrary but is much closer to the real film thickness. In the skeletonized picture, solid grains are then precisely defined from the mask obtained in (i). The skeletonized image is then inverted and a segmentation function of Matlab is used to identify the various bubbles and record their positions and areas (Figure 2d). Finally, we use a tracking algorithm to track each bubble between one image and the image recorded at the next acquisition time step. We thus infer bubble displacements during a time step, and from this, their velocities. The average velocity of the bubbles before entering the porous medium and after leaving it (while still in channel $\mathcal{C}$) are very close to each other, as expected. Their mean value V_0 is what we shall denote *velocity in the flow cell* in the following (see Figure 1); the mean interstitial velocity is thus expected to be V_0/ϕ.

2.4. Control Parameters for the Experiments

The parameters that define an experimental run are the following: the mean bubble area before the foam enters the porous medium, A_0, the flux ratio, $\alpha=Q_l/Q_g$, the gas flow rate, Q_g (during foam preparation), the mean foam velocity inside the flow cell, V_0, and the type of surfactant, *ST*. In this study, we present results from 45 experimental runs. The experimental parameters for these experiments are summarized in Table 1.

3. Results

In this section, we describe a set of general phenomena generic to foam flows in porous media. These processes are particularly interesting for applications such as subsurface remediation, but also from a fundamental point of view, since they are due to the peculiar nature of the foam and are not observed with Newtonian fluids. In this section, we often take some specific experiments as typical examples to illustrate the general phenomena involved, but we also perform a parametric study of the impact of the various control parameters on the investigated processes.

3.1. Preferential Flow Paths

Figure 4 (top) shows a snapshot of the flowing foam structure during experiment number 7. The velocity field, averaged over a duration of 100 s, is shown in Figure 4 (middle); preferential flow paths are clearly visible in this experiment. Nonuniform spatial distribution of foam mobility was previously observed by *Nguyen et al.*

Table 1. Control Parameters for the 45 Foam Flow Experiments[a]

Experiment	1	2	3	4	5	6	7
A_0/Σ	2.08	2.38	2.39	2.43	2.45	2.61	2.68
α	1.0	1.0	1.0	1.0	47.6	47.6	37.9
Q_g	28.3	28.3	28.3	28.3	22.5	22.5	28.3
V_0	1.34	3.44	0.82	1.44	0.75	1.75	2.54
ST	2	1	1	1	1	1	1
Experiment	8	9	10	11	12	13	14
A_0/Σ	3.16	3.18	3.19	3.35	3.44	3.49	3.94
α	21.4	21.4	21.4	21.4	1.5	1.5	1.5
Q_g	50.0	50.0	50.0	50.0	100.0	100.0	100.0
V_0	0.99	2.66	1.77	3.27	3.78	8.47	4.16
ST	1	1	1	1	2	1	2
Experiment	15	16	17	18	19	20	21
A_0/Σ	3.95	3.96	3.97	3.98	3.99	4.06	4.09
α	10.7	10.7	10.7	10.7	6.1	3.1	2.3
Q_g	100.0	100.0	100.0	100.0	100.0	100.0	200.0
V_0	5.11	4.59	3.68	1.12	3.95	4.19	8.07
ST	2	2	2	2	2	2	2
Experiment	22	23	24	25	26	27	28
A_0/Σ	4.11	4.12	4.17	4.25	4.31	4.35	4.36
α	10.7	10.7	10.7	0.6	10.7	1.5	1.5
Q_g	100.0	100.0	100.0	200.0	100.0	100.0	100.0
V_0	4.57	4.03	3.55	8.57	6.50	8.84	3.70
ST	2	2	2	2	2	2	1
Experiment	29	30	31	32	33	34	35
A_0/Σ	4.45	4.50	4.68	4.72	4.76	4.77	5.09
α	1.5	1.5	10.7	10.7	10.7	10.7	1.5
Q_g	100.0	100.0	100.0	100.0	100.0	100.0	100.0
V_0	1.84	0.44	1.78	3.49	0.99	2.76	6.61
ST	1	1	1	1	1	1	1
Experiment	36	37	38	39	40	41	42
A_0/Σ	5.13	5.15	5.37	5.39	5.43	5.52	5.54
α	1.5	1.1	1.5	1.5	10.7	10.7	10.7
Q_g	100.0	200.0	100.0	100.0	100.0	100.0	100.0
V_0	3.68	10.46	0.84	1.71	5.41	5.53	5.41
ST	1	2	1	1	2	2	2
Experiment	43	44	45				
A_0/Σ	6.22	6.31	6.48				
α	10.7	5.1	10.7				
Q_g	100.0	100.0	100.0				
V_0	6.33	20.57	6.13				
ST	2	2	2				

[a]The parameters are the ratio A_0/Σ of the initial mean bubble area to the characteristic size of the pores; the flux ratio α (here in %) and the gas flow rate Q_g (in mL·min^{-1}) used for the foam preparation; the mean foam velocity in the cell, V_0, in mm·s^{-1}; and the type of foaming solution, *ST*.

[2007] using X-ray tomography; they showed qualitatively that preferential flow paths existed. Figure 4 (bottom) shows a map of the pores in which the color for each pore indicates the ratio of its linear size (defined as the square root of its area) to that of the largest pore. A description of how the pores have been determined is given in Appendix A. Visual comparison between the maps of pores and local velocities shows that most preferential paths occur where a series of large pores are connected together. This is analog, for foam flow and at the pore scale, to a Darcy-scale phenomenon well known for water flow in soils: preferential flow generally occurs along paths of permeability larger than the average medium permeability.

The probability density function (PDF) of the velocity field shown in Figure 4 (middle) is shown in Figure 5. The PDF is rather widely distributed for the positive values of V_x, corresponding to the longitudinal flow direction. The inset shows the PDF in a semilogarithmic representation. The concavity of the curve on this plot indicates that the decay of the PDF is faster than an exponential one. The PDF also features a large

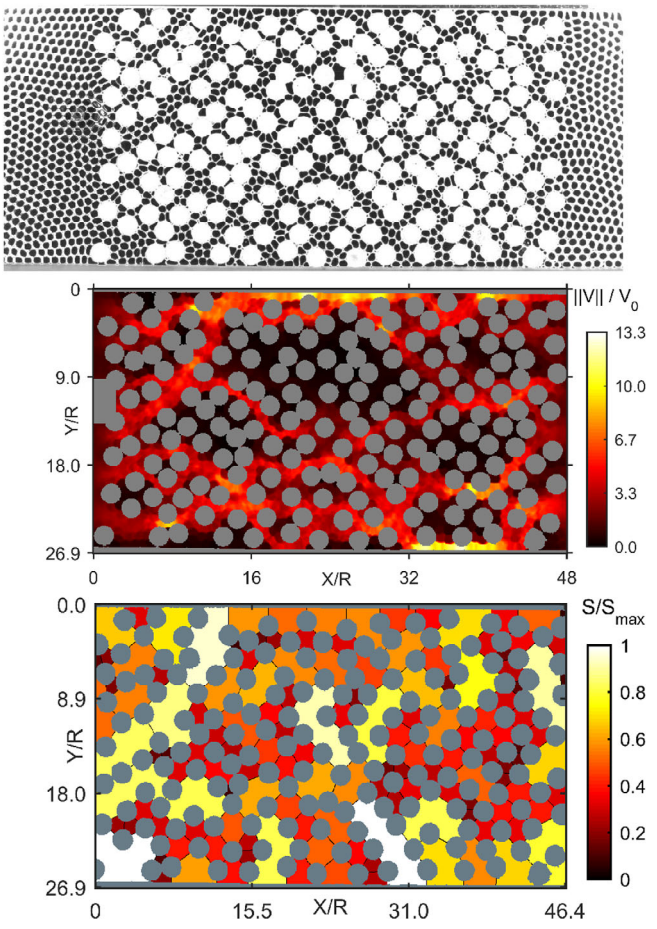

Figure 4. (top) Snapshot of the foam structure during experiment 7 ($A_0/\Sigma = 2.68$, $\alpha = 37.9\%$, $V_0 = 2.54$ mm/s). (middle) Map of normalized bubble velocities, averaged over 100 s, for the same experiment. (bottom) Spatial organization of the pores: the color of the pores indicates their linear size normalized by the linear size of the largest pore.

peak at small velocities, corresponding to bubbles trapped in regions of low flow velocity in-between closely set grains, and which oscillate around their trapping position, hence the negative values of the longitudinal velocity. These bubbles do not contribute to the flow inside the porous medium and play a role equivalent to the obstacles on short time scales. On each image, we define the trapped bubbles as the bubbles with an instantaneous velocity smaller than 0.2 V_0, the other ones being defined as the mobile bubbles. This arbitrary cutoff is qualitatively consistent with our observation of oscillating bubbles. The trapped bubbles in experiment 7 cover about 18% of the free area in the cell. The flow thus behaves as if the *effective* porosity of the porous medium, ϕ_{eff}, was 43% instead of 52%. This has been checked by computing the average velocity of mobile bubbles, $\langle V_x^m \rangle$. Indeed we find $\langle V_x^m \rangle = 2.5\, V_0$ while we expect 1.9 V_0 with a porosity of 52% and 2.3 V_0 with a porosity of 43%.

Finally, note that negative values of V_x can also be recorded for two other reasons: the first one is due to a few errors in the tracking of the bubbles. These events are rare and we estimate that their contribution to the computation leads to an uncertainty on the order of 0.1% on the PDF amplitude. The second one is the presence of regions in which the bubbles have to get around obstacles in such a manner that they happen to flow temporarily backward with respect to the main flow direction.

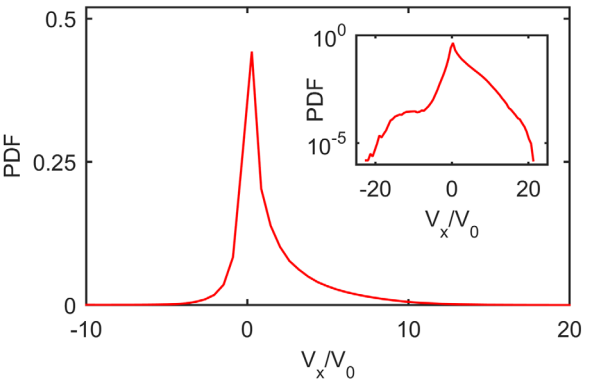

Figure 5. Probability density function of the velocity for experiment 7. The inset shows the PDF in semilogarithmic representation.

3.2. Local Intermittency

Let us now consider experiment number 5, which was performed under conditions identical to those of experiment number 7, except that the mean foam velocity V_0 was more than 3 times lower (see Table 1). Averaging the velocities over a time scale of 1 s, we observe that the velocity map changes with time (see Figure 6). The distribution of fluxes between channels is not permanent; local intermittency of the flow is observed, in spite of the constant, flow-driving, pressure gradient imposed between the inlet and outlet of the flow cell. The local flow intermittency results in fact from strong fluctuations

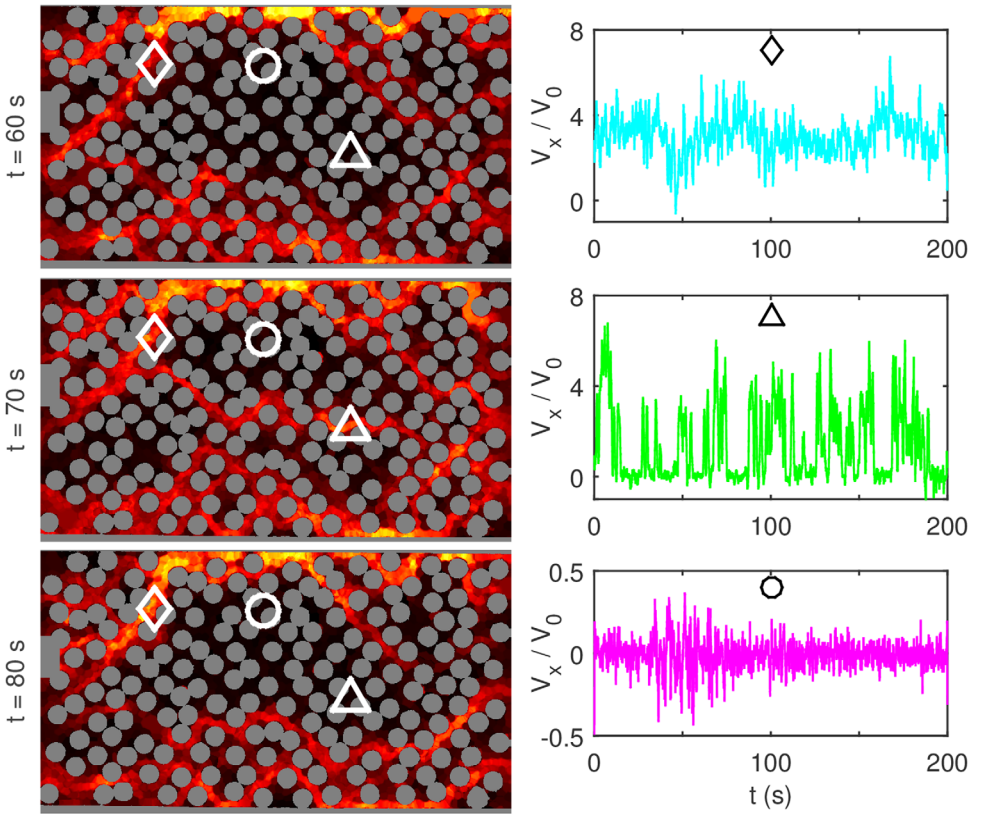

Figure 6. (left column) Example of local intermittency in the distribution of the local preferential channels in experiment 5. The experiment is performed in conditions similar to those of experiment 7, but with an entrance velocity more than 3 times lower. (right column) Evolution of the bubble velocity at the three positions indicated by three symbols on the velocity maps. The velocity maps and time evolutions of velocities are obtained by averaging the measurements over 1 s.

of the local pressure gradient, both in time and space: such fluctuations are essentially a Laplace pressure-related effect, that is, they correspond to fluctuations in time and space of the effective capillary force felt by each bubble. Indeed, when a film is in contact with two obstacles, its shape adapts to fulfill the contact condition at both ends, resulting in a curvature of the film and consequently in a Laplace pressure across the film, or equivalently in a capillary force along the normal to the film; depending on the film concavity, the capillary force can be an additional driving force, or on the contrary, a resisting force. The effective capillary force felt by the bubble is the sum of the capillary forces acting on all films along the bubble perimeter. For a given bubble, it varies in time depending on the geometry of the grains with which the bubble is in contact. From a Eulerian point of view (that is, seen in the fixed coordinate system of the laboratory), this translates into fluctuations in time and space of the local pressure gradient, as mentioned above.

In order to further illustrate this local intermittency, we have sampled the local longitudinal component V_x of the velocity in time, at three positions within the flow field shown in Figure 6: one at which preferential flow is always present (top, cyan line), one at which there is no preferential flow (bottom, pink line), and one at which preferential flow occurs in an intermittent manner (middle, green line). They are plotted in Figure 6 (right column) and are consistent with the visual observations. In the top plot, V_x fluctuates around a mean velocity $V_x = 3.0\ V_0$, while in the bottom plot, it is distributed symmetrically around a zero mean, with fluctuations smaller than $0.4\ V_0$. In the intermediate regime (middle plot), the velocity evolution exhibits alternating periods of very small velocities ($\lesssim 0.1\ V_0$) and positive velocities larger than the global average interstitial velocity $V_0/\phi \simeq 1.9\ V_0$. Note however that in this experiment, V_0 is very low, which results in an uncertainty of about 25% on its estimated value. In order for intermittency to be significant, the imposed pressure drop must not be too large with respect to capillary fluctuations, and therefore the average interstitial velocity must be low.

Intermittency is observed to be more pronounced for smaller bubbles. This is expected in view of the interpretation of intermittency provided above. Since the Laplace pressure across a single film is on the order of γ/r, with

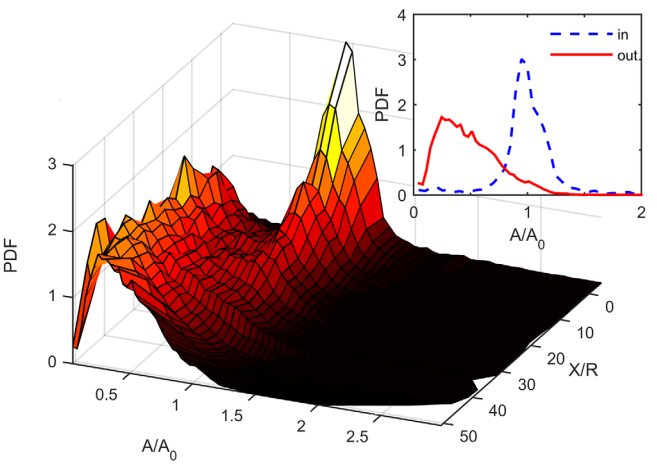

Figure 7. Evolution of the bubble area probability density function (PDF) along the medium, between the initial state (dashed blue line in the inset) and the final state (continuous red line in the inset) in experiment 28 ($A_0/\Sigma = 4.36$, $\alpha = 1.5\%$, $V_0 = 3.70$ mm/s). A/A_0 is the ratio of the bubble area to the initial average bubble area, A_0.

γ being the surface tension coefficient and r the half-distance between the two obstacles (see the inset of Figure 3), the averaging of capillary forces over all films along a bubble perimeter is likely to provide different results depending on the relative magnitudes of the mean bubble size and typical pore size in the medium. Bubbles much larger than the typical size between obstacles are limited by a large number of films in contact with two obstacles; under these conditions, the contribution of the capillary forces through individual films to the effective capillary force felt by one bubble average out statistically, so that the local pressure gradient felt by the bubble equals more or less the global, constant, pressure gradient. Smaller bubbles, on the contrary, are subjected to much larger local pressure fluctuations; in some configurations, capillary forces through individual films may add up along a bubble perimeter to produce a significantly resistive force which is able to overcome the mean driving force associated to the global pressure gradient: the small bubble is then trapped.

3.3. Selection of the Bubble Size Distribution by the Medium

3.3.1. Evolution in Time of the Bubble Size Distribution

For a large enough initial mean bubble size A_0, the outgoing foam is much more polydisperse than the incoming foam. Hence, the probability density function (PDF) for bubble areas evolves along the path through the porous medium. This PDF has been computed in windows of width 50 pixels along the longitudinal direction of the porous medium, which corresponds to an average obstacle diameter plus a constriction width $2(R + r)$. The evolution of the distribution as a function of the longitudinal coordinate (normalized by the typical obstacle radius) is shown in Figure 7 as a three-dimensional plot. As expected, the PDF for the incoming foam (also shown as a blue line in the two-dimensional plot of the inset) is peaked rather symmetrically around the mean bubble size. The PDF for the outcoming foam (also shown as a continuous red line in the 2-D plot of the inset in Figure 7), in contrast, is skewed, with a most probable value about 4 times smaller than that for the incoming foam, and a mean value also more than twice smaller than the incoming mean bubble size. The symmetrical peak of the PDF for the incoming foam (the dashed blue line in the figure inset) decays in time while the outlet distribution (the continuous red line in the figure inset) builds up. Clearly, the initial "mode" disappears while a new distribution, chosen by the medium and much broader, develops.

3.3.2. Size Adjustments Mechanisms

The bubble size distribution evolves under the effect of two mechanisms: lamella division and film breakage.

Lamella division is one of the three classically recognized mechanisms of foam generation in a porous medium [see *Kovscek and Radke*, 1994]. In contrast to the two other mechanisms (leave-behind and capillary snap-off), lamella division can also occur within a preexisting foam flowing through the medium, as illustrated in Figure 8. Let us consider a bubble that is being displaced along a pore whose lateral walls are defined by two grains, the rear film (or lamella) belonging to the bubble is in contact with each grain, on each side. If this film comes in contact with a third grain placed ahead of the two others, it divides into two films, each in its distinct pore. This leads to the formation of two bubbles from the unique bubble colored in red in Figure 8a. The combined area of the two resulting bubbles is identical to that of the initial single bubble within about 0.1%, despite the fact that the pressure within a bubble depends on the curvature radius of its interface and therefore on its size. Indeed, the capillary pressure across a lamella is about 3 orders of magnitude smaller than the pressure on either side of the lamella. The mechanism of bubble

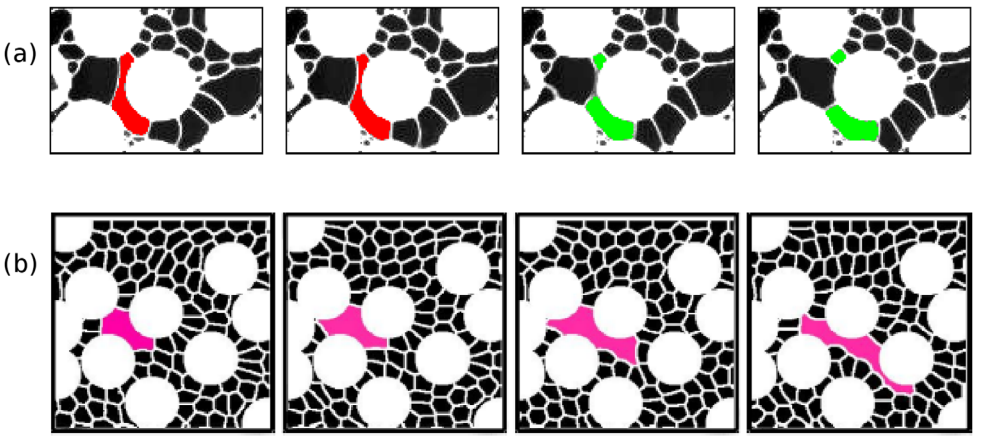

Figure 8. The two mechanisms of bubble size evolution: (a) fragmentation of a bubble by lamella division, and (b) film breakage. In Figure 8a, a bubble is shown just prior to the contact between its rear film and a grain; in Figure 8b, the film breakage triggers an escape of the bubble from the pore where it was initially trapped.

fragmentation resulting from the division of a film (or lamella) appears to be dominant in controlling the time evolution of the bubble size distribution in our system. Note that the effect of this mechanism was recently studied numerically by *Cox* [2015] on a bamboo foam meeting one or several obstacles. A bamboo foam is a foam that circulates in a narrow channel and whose lamellas all span the entire cross section of the channel [*Terriac et al*., 2006]; it corresponds to the simplest possible topology for a foam.

The second mechanism is film breakage, and was less frequently observed than bubble fragmentation in our system. Figure 8b provides an example of configuration in which film breakage provokes the merging of a bubble trapped between three grains and another bubble positioned outside of that "trap." Consequently, further film breakage occurs ahead of the bubble, allowing it to escape the trap.

If one considers that lamella division is the mechanism mainly controlling the evolution of the bubble area PDF shown in Figure 7, each bubble of the incoming foam will, by lamella division, fragment into two bubbles of sizes smaller than their "mother", and the mean bubble size is thus expected to decrease continuously as the foam progresses through the medium, meeting sites with a local geometry appropriate for lamella division. This is consistent with the three-dimensional plot in Figure 7.

Some authors indicate that mechanisms responsible for lamellae creation and destruction in porous media eventually balance each other, leading to a uniform texture of the flowing foam, a property that can be inferred from the near-linear dependence of the pressure drop along the medium as a function of the medium length [e.g., *Pang*, 2010]. In our experiments, we experience very few bubble disappearances according to the mechanisms described in section 1. Indeed, on the one hand bubble coarsening is not observed, even in aggregates of trapped bubbles, because the typical time scale for gas diffusion through the aqueous films remains much larger than the time of completion of our experiment. In any case, it would not be able to compete with the fast occurring bubble fragmentation. On the other hand, since in our porous medium pore throat widths are of the same order as pore sizes, film rupture due to capillary suction is unlikely, except for very large mean velocities that have not been investigated here.

3.3.3. Influence of the Various Parameters on Bubble Size Selection

We have systematically quantified the efficiency of bubble fragmentation, as a function of the experimental parameters presented in Table 1. For that purpose, we define an efficiency of fragmentation as

$$e_{fr} = \frac{A_0 - A_\infty}{A_0}, \tag{4}$$

where A_0 is the bubble size of the incoming foam and A_∞ the mean bubble size measured at the outlet of the porous medium. The fragmentation efficiency is 0 when A_∞ is identical to A_0, and reaches 1 when the A_∞ approaches 0.

In Figure 9, we show the values of e_{fr} for all 45 experiments, represented as a function of the initial average bubble area A_0 in three distinct plots, each one corresponding to one of the following ranges of flux ratio α:

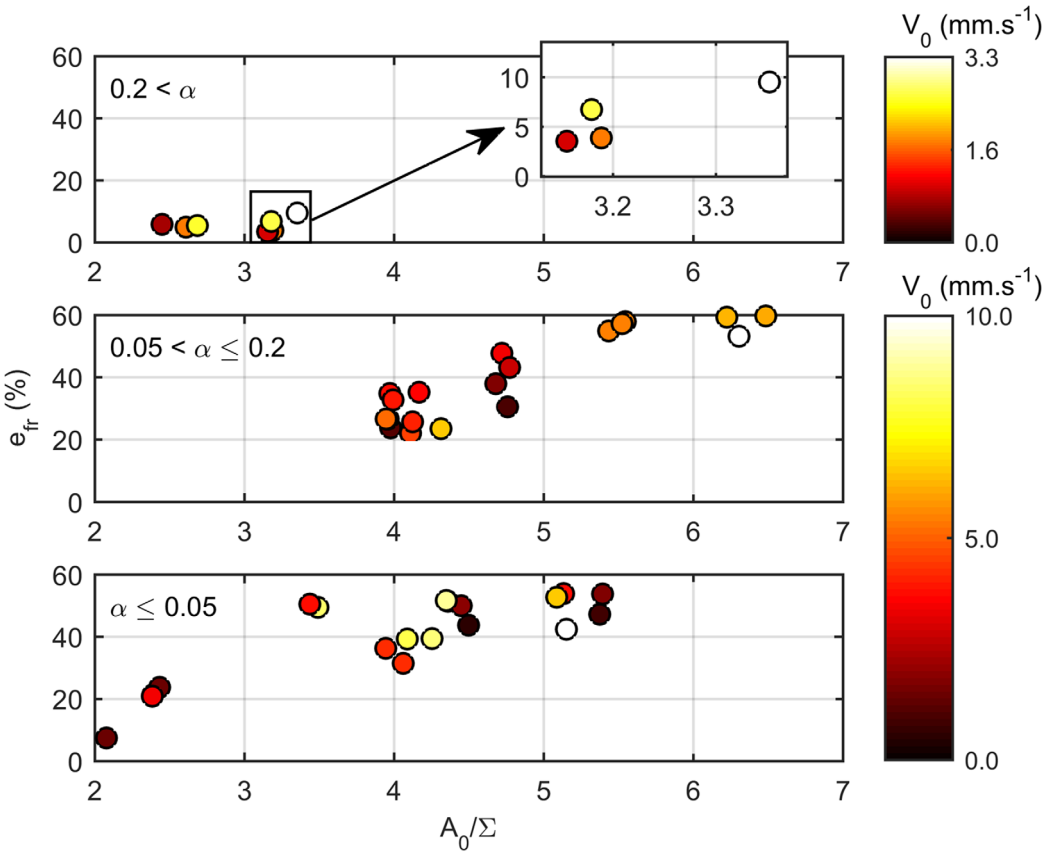

Figure 9. Fragmentation efficiency e_{fr} represented as a function of the mean bubble area of the incoming foam, A_0, normalized by the medium's characteristic length scale, Σ, for three ranges of flux ratio α: $\alpha > 0.2$ (top), $0.05 < \alpha \leq 0.2$ (middle), and $\alpha \leq 0.05$ (bottom). The color of the symbols indicates the entrance velocity V_0 during that experiment.

$\alpha \leq 0.05$ (the driest foams, bottom plot), $0.05 < \alpha < 0.2$ (middle plot), and $\alpha > 0.2$ (the wettest foams, top plot). Each colored disk corresponds to one experiment, and the color scale for the disks indicates the average foam velocity V_0 for the various experiments. We observed that the type of surfactant used for the foam preparation had a negligible impact on the measured fragmentation efficiency, all other parameters being equal. We therefore do not distinguish the types of surfactant in the plots. Notice that our experiments do not span the region of both larger A_0 and larger α values, because the foam generation and injection setup does not allow for a full independent control of bubble size and injection velocity.

This diagram shows that the efficiency depends mostly on the initial mean bubble area A_0 and flux ratio α, which controls the quality of the foam. It appears, within the limits of our sampling of the parameter space, that the fragmentation efficiency increases with the mean incoming bubble area and decreases with the flux ratio (or equivalently, increases with the foam quality). The observed dependence on the incoming bubble area is expected, as larger bubbles are more likely to be subjected to lamella division. Based on this division mechanism, we would also expect that the foam velocity should have little impact on the fragmentation efficiency. This hypothesis seems to be verified by our data, although it cannot easily be tested since experiments performed at different mean foam velocities also often differ in the mean bubble area of the incoming foam or the flux ratio. The influence of the flux ratio α on the fragmentation efficiency can be understood as follows: prior to lamella division, the lamella spans a large gap between two obstacles (Figure 8a), which enforces a significant deformation of the bubble that is about to split. Increasing α, hence increasing the liquid fraction, reduces the maximal deformation that a bubble can undergo before swapping neighbors. In the context of lamella division, it means that the bubbles have a larger probability to escape through one obstacle constriction instead of splitting.

In Figures 10 and 11, we provide examples of how the fragmentation efficiency depends on the foam quality and the mean velocity. In Figures 10a and 10b, we show two foams of similar initial average bubble size but

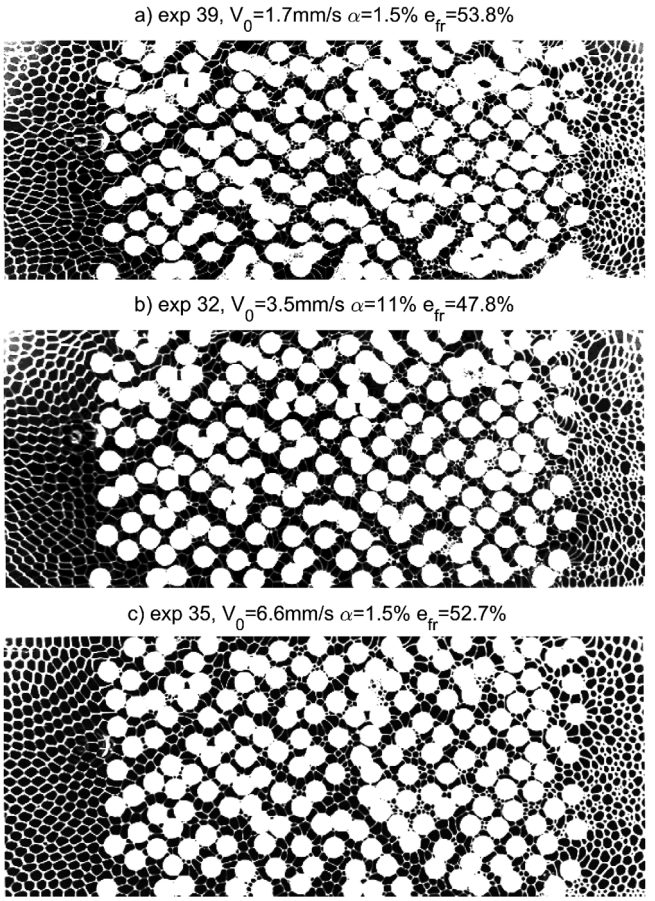

Figure 10. Effect of the initial foam quality and mean foam velocity on the bubble size selection. The corresponding experiments are (from top to bottom) experiments number 39, 32, and 35. A foam of (a) better quality (i.e., drier) is observed to be impacted differently than a foam of (b) lesser quality (i.e., wetter). The comparison of Figures 10a and 10c shows that the entrance velocity V_0 has little influence on the process.

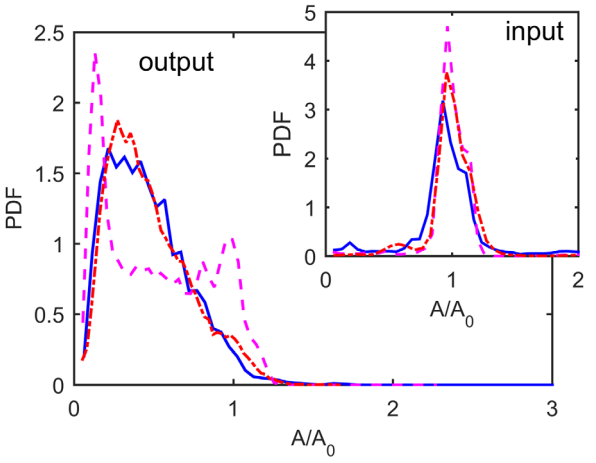

Figure 11. Size distributions recorded at the outlet of the porous medium for the same experiments as in Figure 10. Continuous blue line: same data as Figure 10a, magenta dashed line: same data as Figure 10b, and dashed-dotted red line: same data as Figure 10c. The inset shows the initial size distributions.

different qualities (flux ratio $\alpha = 1.5\%$ for (a) and $\alpha = 10.7\%$ for (b)). The foam of higher quality at the inlet (case (a)) exits the medium with a polydisperse bubble area distribution different from that of the lower-quality counterpart, as quantitatively shown in Figure 11. Figure 10c shows the same foam as the one of Figure 10a, but at a larger mean velocity ($V_0 = 1.71$ mm/s for (a) and $V_0 = 6.61$ mm/s for (c)). The polydispersity of the foam exiting the medium exhibits little dependence on the foam mean velocity. Those observations are consistent with the general behavior discussed in the previous paragraph.

3.4. Correlation Between Local Velocities and Bubble Sizes

Another important feature observed in our foam flows is the link between the bubbles' mobility and their size. Figure 12a shows a snapshot of experiment number 43, where different bubble areas can clearly be identified. The corresponding map of bubble sizes is shown in Figure 12b, and the corresponding normalized velocity field, integrated over 100 s, in Figure 12c. Visual comparison between the two suggests that larger bubbles follow paths of faster flow while smaller bubbles exhibit a smaller mobility, and can in particular be trapped in-between tightly set groups of three or four grains.

In order to investigate the correlations between bubble sizes and velocities quantitatively, we compare the velocity PDF for bubbles with areas larger than the average bubble area $\langle A \rangle$ (red crosses in Figure 13) to those for bubbles with areas smaller than $\langle A \rangle$ (blue solid circles in Figure 13). The velocity PDF for bubbles smaller than the average has more weight on low velocities than that for bubbles larger than the average. The velocity at which the population of larger bubbles starts dominating over that of smaller bubbles is 1.8 V_0, very close to the expected interstitial velocity V_0/ϕ. This analysis shows that small bubbles may

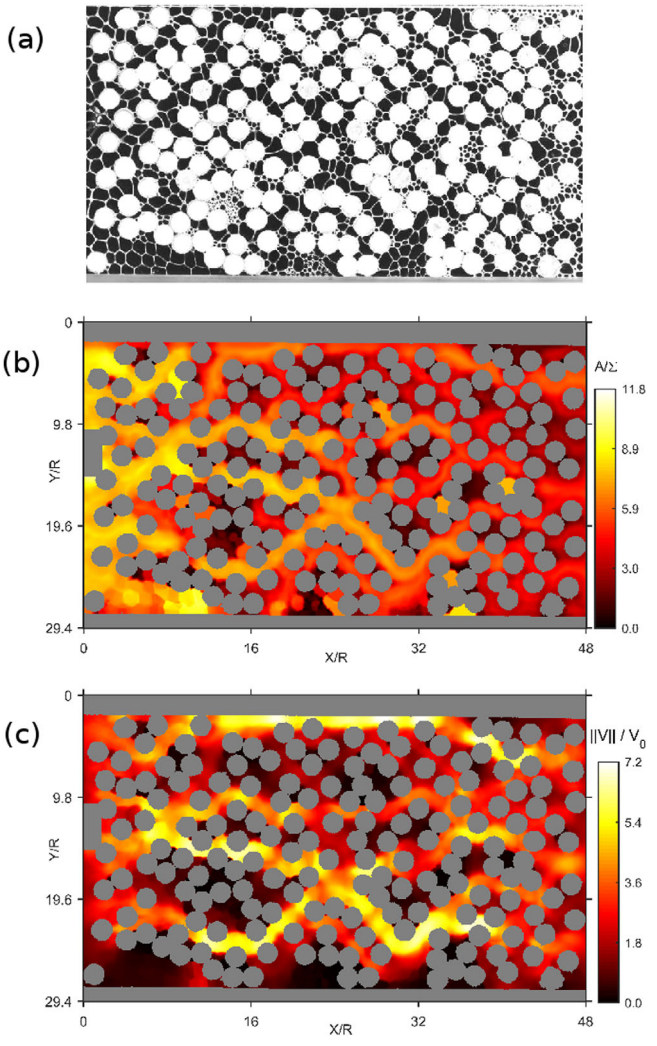

Figure 12. (a) Snapshot of experiment 43 ($A_0/\Sigma = 6.22$, $\alpha = 10.7\%$, $V_0 = 6.33$ mm/s). (b) Maps of normalized bubble sizes for the same experiment. (c) Maps of normalized bubble velocities.

flow faster than the mean flow velocity V_0/ϕ, but most of them flow slower, while the biggest bubbles show the opposite behavior.

A more systematic study of the correlation between bubble sizes and velocities as a function of the various experimental control parameters is based on the cross-correlation coefficient $C_{AV,}$ whose definition is given in Appendix B. In Figure 14, we show how the cross-correlation coefficient depends on the foam's polydispersity, (i.e., the relative width of the bubble area distribution, see Appendix B), for experiments with various flux ratios α indicated by the size of the symbols and fragmentation rates e_{fr} indicated by the color of the symbols. The positive value of $C_{AV,}$ observed for the entire data, evidences that the largest bubbles move, on average, faster than the mean flow. This effect is more pronounced at high size polydispersity, or, equivalently, high fragmentation efficiency. Figure 14 also evidences that the correlation between bubble sizes and velocities is all the larger as the foam is drier. Note that in our experiment, the liquid fraction and the size polydispersity (or, equivalently, the fragmentation efficiency) are correlated variables. This was shown in Figure 9 and is also apparent in Figure 14 where larger symbols have a darker color. Drier foams get more fragmented and reach a higher level of polydispersity, whereas the more monodisperse foams are the wetter ones. Thus, strictly speaking, we do not know whether the enhanced correlation between bubble size and velocity observed at large polydispersity in Figure 14 is due to the polydispersity in itself, or whether it is a consequence of the smaller liquid fraction.

Overall, this study demonstrates that larger bubbles are more likely to flow faster than smaller ones, but that this effect is only significant for sufficiently dry foams.

4. Summary and Conclusion

We have studied the flow of a preexisting two-dimensional foam inside a porous medium consisting of cylindrical solid grains, under conditions of discontinuous gas flow in the entire medium. Our experimental setup allows a direct visualization and quantitative analysis of phenomena previously reported for foam flow in porous media: preferential flow paths, flow intermittency, bubble trapping. Preferential flow paths were analyzed from the measurement of the full bubble velocity field. A significant portion of the bubble population was found to flow at velocities up to 4 times the mean interstitial velocity. Flow intermittency was shown to consist in a time evolution of the preferential flow paths' geometry, some of these paths being permanent and others being either active or inactive, depending on the time at which they are being observed. Furthermore, the distribution

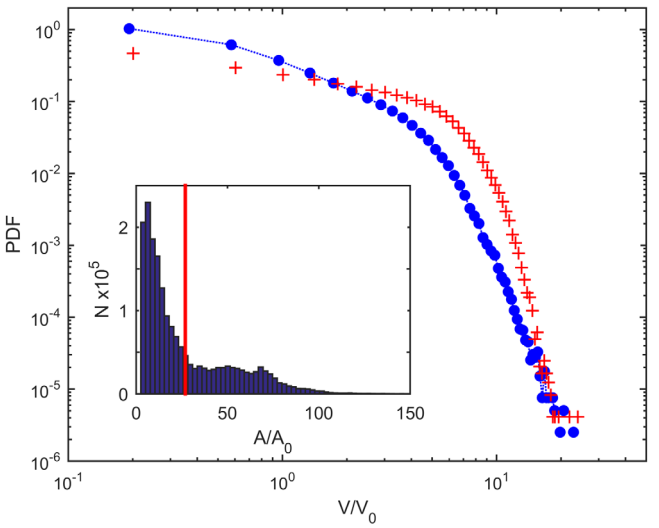

Figure 13. Probability distribution function (PDF) of the velocity field for bubbles of area in the ranges $0 \leq A \leq \langle A \rangle$ (blue solid circles) and $A > \langle A \rangle$ (red crosses), where $\langle A \rangle$ is the average normalized bubble size computed on the area map of Figure 12. The inset shows a histogram of the bubble areas, with $\langle A \rangle / A_0$ indicated by a vertical red line.

of bubble sizes was observed to evolve monotonically between the system inlet and its outlet, from the inlet symmetrical quasi-monodisperse probability density function (PDF) to a PDF with a skewed peak of most probable bubble size about 4 times smaller than the mean bubble size at the inlet. This systematic evolution toward smaller bubble sizes is consistent with the dominant bubble size evolution mechanism, namely bubble fragmentation by lamella division. A spatial correlation between bubble sizes and velocities was evidenced. The efficiency of the bubble fragmentation, as well as the correlation between bubble sizes and velocities, were measured as a function of various control parameters: the mean bubble size at the inlet, the foam quality, the mean flow velocity, and the type of surfactant used in the formulation of the foaming solution. The fragmentation efficiency depends mostly on the initial mean bubble size and foam quality; larger qualities and larger velocities enhance the foam polydispersity.

The correlation between bubble sizes and velocities has an important consequence in terms of foam rheology, which has been overlooked until now: in the relationship between the mean interstitial velocity and the pressure drop (equation (2)), the parameter β is proportional to the number of foam bubbles per unit volume [*Kovscek and Bertin*, 2003b], that is, for a 2-D foam, inversely proportional to the mean bubble area, so the prefactor in that equation is proportional to the mean bubble area. Since the mean bubble area in the channels of preferential flow is significantly larger than the global mean bubble area, the prefactor in equation (2) actually contains an implicit increasing dependence on the mean interstitial velocity v. Overall this weakens the dependence of v on the pressure drop and decreases the deviation of the foam's effective rheology from that of a Newtonian fluid. This behavior is expected to also be observed for 3-D foams flowing in subsurface porous media, and this all the more for media that are very heterogeneous and multiscale, and exhibiting preferential flows. The remediation of soils is among the applications in which this rheological property is expected to play a significant role. More generally, this study opens the way to quantitative characterization of the relationship between medium geometry and foam flow phenomenology. One possible application of this finding would be in large-scale models of subsurface foam flows: it could be beneficial to develop models that not only consider the dependence on the local velocity of the effective viscosity of the foam, but also explicitly account for the spatial distribution of bubble sizes

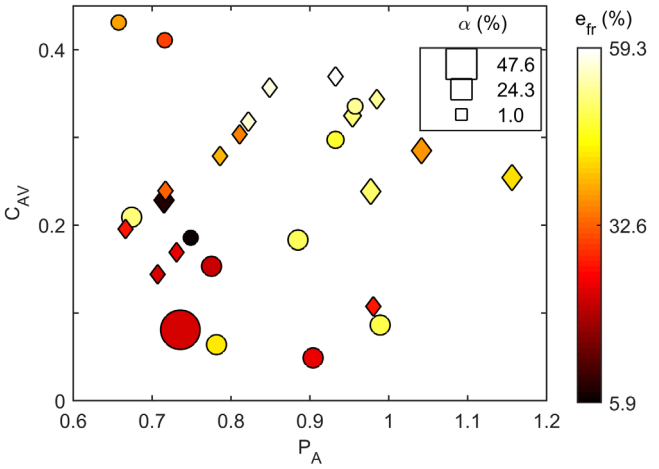

Figure 14. Evolution of the cross-correlation coefficient C_{AV} with the mean polydispersity P_A of the porous medium. Each experiment is represented by a symbol whose color indicates the value of e_{fr} and whose size indicates the flux ratio α. Two types of symbols are plotted: circles for experiments performed with solution 1, and diamonds for experiments performed with solution 2. The black squares indicate symbol areas corresponding to flux ratio values $\alpha = 1.0\%$, 24.3%, and 47.6%.

and the coupling between the local permeability of the medium and the effective viscosity of the foam (through the coupling of the permeability and the bubble size).

Remember though that in our system, mechanisms of bubble disappearance are quasi-inexistant: over the investigated time scale, foam coarsening by gas diffusion is negligible, while the ratio of the average pore size to the average pore neck size is not large enough to allow capillary suction to cause lamella rupture. Hence the bubble size distribution does not evolve toward a stationary state where mechanisms of lamella creation and destruction would balance each other. Future works will tackle the size selection mechanism in medium geometries with much more marked constrictions between pores, as well as in media with a different dimensionality, such as porous media columns commonly used by soil physicists and three-dimensional sand tanks. Another prospect is the modeling of the fragmentation process and its confrontation to the PDFs measured experimentally in the present study.

Appendix A: Pore Map Determination

The pore map of Figure 4 (bottom) is obtained in the following manner. A Delaunay triangulation is performed on the image that defines the grain (see red segments in Figure 2b). Then a number of these segments are removed selectively, and the pores are defined as the resulting continuous black areas. The segments removed are those which are significantly longer than their nearest neighbors: each segment $\mathcal{S}$ is selected for removal, or not, from a comparison of its length with respect to that of the four other segments constituting the two triangles that share the segment $\mathcal{S}$. More precisely, we compute the ratio of the length of $\mathcal{S}$ to the average length of the two shortest such segments. Performing this measurement on all segments, plotting the PDF of these "length ratios" provides a distribution with two weakly separated peaks, indicating two populations of segments. The segments belonging to the right peak (i.e., with the larger length ratios) were removed.

Appendix B: Definition of the Cross Correlation Between Bubble Sizes and Velocities

The cross-correlation coefficient between bubble sizes and velocities, $C_{AV,}$ is computed as follows. From the average area and velocity maps, we compute the average bubble size $\langle A\rangle$ and the standard deviation σ_A of bubble area values about $\langle A\rangle$, as well as the corresponding quantities for velocities, $\langle V\rangle$ and σ_V, respectively. The cross correlation is then given by:

$$C_{AV}=\frac{\langle \tilde{A}\tilde{V}\rangle}{\sigma_A\sigma_V}\,, \tag{B1}$$

with $\tilde{A}=A-\langle A\rangle$ and $\tilde{V}=V-\langle V\rangle$. We also define a measure of the polydispersity of the foam flowing inside the porous medium, by the ratio $P_A=\sigma_A/\langle A\rangle$. Note that we only process the data from the bubbles positioned inside the porous medium.

The coefficient C_{AV} is normalized to be of order unity. In Figure 14, its measured values are all positive, and around $C_{AV}=0.24\pm0.11$. This value indicates a rather weak correlation, which can be understood by looking at Figure 12, in which the average bubble size clearly decays throughout the channel; at the end of the channel, the size of the fastest bubbles corresponds to the size of the slowest ones at the entrance. The cross-correlation coefficient is then low since it is computed over all bubbles in the channels, not taking into account the decrease of the average bubble size along the length of the porous medium.

Acknowledgments
The authors acknowledge financial support from Région Bretagne (CREATE MOUSPORE). Y.M. is grateful to H. Bertin and L. Zhong for enlightening discussions. B.G. and B.D. thank Claire Bocher for experimental help. The authors commit to making their data available to any reader who requires it, once all results to be obtained from the data have been published.

References

Alvarez, J., H. Rivas, and W. Rossen (2001), Unified model for steady-state foam behavior at high and low foam qualities, *SPE J.*, *6*(03), 325–333.
Apaydin, O. G., and A. R. Kovscek (2001), Surfactant concentration and end effects on foam flows in porous media, *Transp. Porous Media*, *43*(3), 511–536.
Aronson, A., V. Bergeron, M. E. Fagan, and C. Radke (1994), The influence of disjoining pressure on foam stability and flow in porous media, *Colloids Surf. A*, *83*(2), 109–120.
Bretherton, F. (1961), The motion of long bubbles in tubes, *J. Fluid Mech.*, *10*(02), 166–188.
Cantat, I., N. Kern, and R. Delannay (2004), Dissipation in foam flowing through narrow channels, *Europhys. Lett.*, *65*(5), 726–732.
Cantat, I., S. Cohen-Addad, F. Elias, F. Graner, R. Hœhler, O. Pitois, F. Rouyer, and A. Saint-Jalmes (2013), *Foams. Structure and Dynamics*, translated by Ruth Flatman, Oxford Univ. Press, Oxford, U. K.
Chen, M., Y. Yortsos, and W. Rossen (2005), Insights on foam generation in porous media from pore-network studies, *Colloids Surf. A*, *256*(2), 181–189.

Chowdiah, P., B. R. Misra, J. J. Kilbane, V. J. Srivastava, and T. D. Hayes (1998), Foam propagation through soils for enhanced in situ remediation, *J. Hazard. Mater.*, *62*, 265–280.
Cohen, D., T. Patzek, and C. Radke (1997), Onset of mobilization and the fraction of trapped foam in porous media, *Transp. Porous Media*, *28*(3), 253–284.
Cox, S. (2015), Simulations of bubble division in the flow of a foam past an obstacle in a narrow channel, *Colloids Surf. A*, *473*, 104–108.
Cox, S. J., S. Neethling, W. R. Rossen, W. Schleifenbaum, P. Schmidt-Wellenburg, and J. J. Cilliers (2004), A theory of the effective yield stress of foam in porous media: The motion of soap film traversing a three-dimensional pore, *Colloid. Surf. A*, *245*(1–3), 143–151.
Denkov, N. D., V. Subramanian, D. Gurovich, and A. Lips (2005), Wall slip and viscous dissipation in sheared foams: Effect of surface mobility, *Colloids Surf. A*, *263*(1), 129–145.
Dholkawala, Z. F., H. Sarma, and S. Kam (2007), Application of fractional flow theory to foams in porous media, *J. Pet. Sci. Eng.*, *57*(1), 152–165.
Dollet, B., and C. Raufaste (2014), Rheology of aqueous foams, *C. R. Phys.*, *15*(8), 731–747.
Dollet, B., S. A. Jones, Y. Méheust, and I. Cantat (2014), Influence of the elastic deformation of a foam on its mobility in a model porous medium, *Phys. Rev. E*, *90*, 023006.
Drenckhan, W., S. Cox, G. Delaney, H. Holste, D. Weaire, and N. Kern (2005), Rheology of ordered foams—On the way to discrete microfluidics, *Colloids Surf. A*, *263*(1), 52–64.
Du, D.-X., A. N. Beni, R. Farajzadeh, and P. L. Zitha (2008), Effect of water solubility on carbon dioxide foam flow in porous media: An x-ray computed tomography study, *Ind. Eng. Chem. Res.*, *47*(16), 6298–6306.
Falls, A., J. Musters, and J. Ratulowski (1989), The apparent viscosity of foams in homogeneous bead packs, *SPE Reservoir Eng.*, *4*(02), 155–164.
Fergui, O., H. Bertin, and M. Quintard (1998), Transient aqueous foam flow in porous media: Experiments and modeling, *J. Pet. Sci. Eng.*, *20*(1), 9–29.
Ferguson, D., and S. Cox (2013), The motion of a foam lamella traversing an idealised bi-conical pore with a rounded central region, *Colloids Surf. A*, *438*, 56–62.
Friedmann, F., W. Chen, and P. Gauglitz (1991), Experimental and simulation study of high-temperature foam displacement in porous media, *SPE Reservoir Eng.*, *6*(01), 37–45.
Gauglitz, P., and C. Radke (1990), The dynamics of liquid film breakup in constricted cylindrical capillaries, *J. Colloid Interface Sci.*, *134*(1), 14–40.
Heller, J. P., and M. S. Kuntamukkula (1987), Critical review of the foam rheology literature, *Ind. Eng. Chem. Res.*, *26*(2), 318–325.
Hirasaki, G., and J. B. Lawson (1985), Mechanisms of foam flow in porous media: Apparent viscosity in smooth capillaries, *SPEJ Soc. Pet. Eng. J.*, *25*(02), 176–190.
Hirasaki, G., et al. (1997), Field demonstration of the surfactant/foam process for aquifer remediation, in *SPE Annual Technical Conference and Exhibition paper SPE 39292 presented at SPE Annual Technical Conference 698 and Exhibition*, Soc. of Pet. Eng., San Antonio, Tex.
Huang, C.-W., and C.-H. Chang (2000), A laboratory study on foam-enhanced surfactant solution flooding in removing n-pentadecane from contaminated columns, *Colloids Surf. A*, *173*(1), 171–179.
Huang, D. D., A. Nikolov, and D. T. Wasan (1986), Foams: Basic properties with application to porous media, *Langmuir*, *2*(5), 672–677.
Jenkins, K. B., D. L. Michelsen, and J. T. Novak (1993), Application of oxygen microbubbles for in situ biodegradation of p-xylene-contaminated groundwater in a soil column, *Biotechnol. Prog.*, *9*(4), 394–400.
Jeong, S.-W., and M. Y. Corapcioglu (2003), A micromodel analysis of factors influencing napl removal by surfactant foam flooding, *J. Contam. Hydrol.*, *60*(1), 77–96.
Jeong, S.-W., and M. Y. Corapcioglu (2005), Force analysis and visualization of napl removal during surfactant-related floods in a porous medium, *J. Hazard. Mater.*, *126*(1), 8–13.
Jeong, S.-W., M. Y. Corapcioglu, and S. E. Roosevelt (2000), Micromodel study of surfactant foam remediation of residual trichloroethylene, *Environ. Sci. Technol.*, *34*(16), 3456–3461.
Jones, S. A., B. Dollet, Y. Méheust, S. J. Cox, and I. Cantat (2013), Structure-dependent mobility of a dry aqueous foam flowing along two parallel channels, *Phys. Fluids*, *25*, 063101.
Kam, S., and W. Rossen (2003), A model for foam generation in homogeneous media, *SPE J.*, *8*(04), 417–425.
Khatib, Z., G. Hirasaki, and A. Falls (1988), Effects of capillary pressure on coalescence and phase mobilities in foams flowing through porous media, *SPE Reservoir Eng.*, *3*(03), 919–926.
Kornev, K. G., A. V. Neimark, and A. N. Rozhkov (1999), Foam in porous media: Thermodynamic and hydrodynamic peculiarities, *Adv. Colloid Interface Sci.*, *82*(1), 127–187.
Kovscek, A., T. Patzek, and C. Radke (1995), A mechanistic population balance model for transient and steady-state foam flow in boise sandstone, *Chem. Eng. Sci.*, *50*(23), 3783–3799.
Kovscek, A., G.-Q. Tang, and C. Radke (2007), Verification of roof snap off as a foam-generation mechanism in porous media at steady state, *Colloids Surf. A*, *302*(1), 251–260.
Kovscek, A. R., and H. J. Bertin (2003a), Foam mobility in heterogeneous porous media (II: Experimental observations), *Transp. Porous Media*, *52*, 37–49.
Kovscek, A. R., and H. J. Bertin (2003b), Foam mobility in heterogeneous porous media (I: Scaling concepts), *Transp. Porous Media*, *52*, 17–35.
Kovscek, A. R., and C. J. Radke (1994), Fundamentals of foam transport in porous media, in *Foams: Fundamentals and Applications in the Petroleum Industry*, edited by L. L. Schramm, chap. 3, pp. 115–163, ACS Publ., Washington, D. C.
Ma, K., R. Liontas, C. A. Conn, G. J. Hirasaki, and S. L. Biswal (2012), Visualization of improved sweep with foam in heterogeneous porous media using microfluidics, *Soft Matter*, *8*(41), 10,669–10,675.
Marmottant, P., and J.-P. Raven (2009), Microfluidics with foams, *Soft Matter*, *5*(18), 3385–3388.
Nguyen, Q. P., P. K. Currie, M. Buijse, and P. L. Zitha (2007), Mapping of foam mobility in porous media, *J. Pet. Sci. Eng.*, *58*(1), 119–132.
Pang, Z.-X. (2010), The blocking ability and flowing characteristics of steady foams in porous media, *Transp. Porous Media*, *85*(1), 299–316.
Patzek, T. W. (1996), Field applications of steam foam for mobility improvement and profile control, *SPE Reservoir Eng.*, *11*(02), 79–86.
Raufaste, C., A. Foulon, and B. Dollet (2009), Dissipation in quasi-two-dimensional flowing foams, *Phys. Fluids*, *21*, 053102.
Raven, J.-P., and P. Marmottant (2009), Microfluidic crystals: Dynamic interplay between rearrangement waves and flow, *Phys. Rev. Lett.*, *102*(8), 084501.
Roof, J. (1970), Snap-off of oil droplets in water-wet pores, *Soc. Pet. Eng. J.*, *10*(01), 85–90.
Rossen, W. R. (1990), Theory of mobilization pressure gradient of flowing foams in porous media: III. *Asymmetric lamella shapes, J. Colloid Interface Sci.*, *136*(1), 38–53.
Rothmel, R. K., R. W. Peters, E. St. Martin, and M. F. DeFlaun (1998), Surfactant foam/bioaugmentation technology for in situ treatment of tce-dnapls, *Environ. Sci. Technol.*, *32*(11), 1667–1675.

Roy, D., S. Kongara, and K. Valsaraj (1995a), Application of surfactant solutions and colloidal gas aphron suspensions in flushing naphthalene from a contaminated soil matrix, *J. Hazard. Mater.*, *42*(3), 247–263.
Roy, D., R. R. Kommalapati, K. T. Valsaraj, and W. D. Constant (1995b), Soil flushing of residual transmission fluid: Application of colloidal gas aphron suspensions and conventional surfactant solutions, *Water Res.*, *29*(2), 589–595.
Shen, X., L. Zhao, Y. Ding, B. Liu, H. Zeng, L. Zhong, and X. Li (2011), Foam, a promising vehicle to deliver nanoparticles for vadose zone remediation, *J. Hazard. Mater.*, *186*, 1773–1780.
Simjoo, M., Q. Nguyen, and P. Zitha (2012), Rheological transition during foam flow in porous media, *Ind. Eng. Chem. Res.*, *51*(30), 10,225–10,231.
Simjoo, M., Y. Dong, A. Andrianov, M. Talanana, and P. Zitha (2013), Ct scan study of immiscible foam flow in porous media for enhancing oil recovery, *Ind. Eng. Chem. Res.*, *52*(18), 6221–6233.
Stevenson, P. (2012), *Foam Engineering: Fundamentals and Applications*, John Wiley, Hoboken, N. J.
Szafranski, R., J. Lawson, G. Hirasaki, C. Miller, N. Akiya, S. King, R. Jackson, H. Meinardus, and J. Londergan (1998), Surfactant/foam process for improved efficiency of aquifer remediation, *Prog. Colloid Polymer Sci.*, *111*, 162–167.
Terriac, E., J. Etrillard, and I. Cantat (2006), Viscous force exerted on a foam at a solid boundary: Influence of the liquid fraction and of the bubble size, *Europhys. Lett.*, *74*(5), 909–915.
Wan, J., J. L. Wilson, and T. L. Kieft (1994), Influence of the gas-water interface on transport of microorganisms through unsaturated porous media, *Appl. Environ. Microbiol.*, *60*(2), 509–516.
Wang, S., and C. N. Mulligan (2004), An evaluation of surfactant foam technology in remediation of contaminated soil, *Chemosphere*, *57*(9), 1079–1089.
Weaire, D. (2008), The rheology of foam, *Curr. Opin. Colloid Interface Sci.*, *13*(3), 171–176.
Weaire, D., and S. Hutzler (1999), *The Physics of Foams*, Oxford Univ. Press., Oxford, U. K.
Wong, H., C. J. Radke, and S. Morris (1995), The motion of long bubbles in polygonal capillaries. Part 2. Drag, fluid pressure and fluid flow, *J. Fluid Mech.*, *292*, 95–110.
Zhdanov, S. A., A. Amiyan, L. M. Surguchev, L. M. Castanier, and J. E. Hanssen (1996), Application of foam for gas and water shut-off: Review of field experience, paper SPE 36914-MS presented at European Petroleum Conference, Soc. of Pet. Eng., Milan, Italy.
Zhong, L., N. P. Qafoku, J. E. Szecsody, P. E. Dresel, and Z. F. Zhang (2009), Foam delivery of calcium polysulfide to the vadose zone for chromium (vi) immobilization: A laboratory evaluation, *Vadose Zone J.*, *8*(4), 976–985.
Zhong, L., J. Szecsody, F. Zhang, and S. M. Mattigod (2010), Foam delivery of amendments for vadose zone remediation: Propagation performance in unsaturated sediments, *Vadose Zone J.*, *9*, 757–767.
Zhong, L., J. Szecsody, M. Oostrom, M. Truex, X. Shen, and X. Li (2011), Enhanced remedial amendment delivery to subsurface using shear thinning fluid and aqueous foam, *J. Hazard. Mater.*, *191*, 249–257.
Zitha, P., Q. Nguyen, P. Currie, and M. Buijse (2006), Coupling of foam drainage and viscous fingering in porous media revealed by x-ray computed tomography, *Transp. Porous Media*, *64*, 301–313.